Subthreshold resonance properties contribute to the efficient coding of auditory spatial cues

Michiel W. H. Remme[a,b,1], Roberta Donato[c,1], Jason Mikiel-Hunter[a,c], Jimena A. Ballestero[c], Simon Foster[c], John Rinzel[a,d], and David McAlpine[c,2]

[a]Center for Neural Science, New York University, New York, NY 10003; [b]Institute for Theoretical Biology, Humboldt-Universität zu Berlin, 10115 Berlin, Germany; [c]University College London Ear Institute, University College London, London WC1X 8EE, United Kingdom; and [d]Courant Institute of Mathematical Sciences, New York University, New York, NY 10012

Neurons in the medial superior olive (MSO) and lateral superior olive (LSO) of the auditory brainstem code for sound-source location in the horizontal plane, extracting interaural time differences (ITDs) from the stimulus fine structure and interaural level differences (ILDs) from the stimulus envelope. Here, we demonstrate a postsynaptic gradient in temporal processing properties across the presumed tonotopic axis; neurons in the MSO and the low-frequency limb of the LSO exhibit fast intrinsic electrical resonances and low input impedances, consistent with their processing of ITDs in the temporal fine structure. Neurons in the high-frequency limb of the LSO show low-pass electrical properties, indicating they are better suited to extracting information from the slower, modulated envelopes of sounds. Using a modeling approach, we assess ITD and ILD sensitivity of the neural filters to natural sounds, demonstrating that the transformation in temporal processing along the tonotopic axis contributes to efficient extraction of auditory spatial cues.

auditory system | superior olivary nucleus | spatial listening

The auditory system analyzes sounds over different time scales to extract ecologically relevant information, including the identity and location of a sound source (Fig. 1A; also see ref. 1). In particular, sensitivity to rapidly fluctuating signals in the temporal fine structure (TFS; the sound-pressure waveform) of sounds enables the extraction of spatial information in the form of interaural time differences (ITDs), i.e., the time difference in the arrival of the stimulus to both ears. For frequencies below about 1,500 Hz, human listeners can discriminate ITDs of just a few tens of microseconds (2–4), corresponding to a spatial resolution of about two degrees for sources located to the front. Such exquisite sensitivity relies on the ability of cochlear hair cells to generate action potentials in auditory nerve fibers that are phase-locked to the instantaneous sound-pressure waveform at each eardrum (Fig. 1A, bottom right). Phase-locking to the TFS in nerve fibers extends to at least 4 kHz in many mammalian species but starts to degrade from about 1 kHz as the result of low-pass filtering by the sensory hair cells (5). Postsynaptic specializations in subsequent stages of the ascending pathway—such as the cochlear nucleus—may improve temporal locking of action potentials to the TFS, at least for frequencies below 1 kHz (6). Phase-locked excitatory (and potentially inhibitory) inputs from each ear ("EE" input) ultimately converge on neurons in the medial superior olive (MSO) of the brainstem, where ITDs are explicitly computed (Fig. 1B).

For sounds above a few kilohertz in frequency, differences in the intensity of the sound at each ear (interaural level differences, ILDs)—generated by the head "shadowing" the ear further from the source—become increasingly important as localization cues. Although phase-locking of action potentials to the TFS typically is absent in this frequency range, the spiking activity does vary with the more-slowly varying sound amplitude (the sound "envelope"). Besides conveying the structure of speech (<10 Hz) and the pitch of complex sounds (e.g., 100–300 Hz for human voice), sensitivity to the sound envelope creates an additional localization cue in the form of the "envelope ITD." Envelope ITDs generally are considered less important than ILDs as a localization cue at these frequencies (7); however, depending on the stimulus parameters and listening conditions, sensitivity to envelope ITDs may approach that observed for ITDs conveyed in the TFS of low-frequency sounds behaviorally (3) and physiologically (8). High-frequency inputs from both ears converge in the lateral superior olive (LSO), where both ILDs and envelope ITDs are computed (Fig. 1B). LSO neurons receive a direct excitatory input from the ipsilateral cochlear nucleus, whereas input from the other ear is inhibitory and reaches the LSO via an intermediate synapse from the medial nucleus of the trapezoid body (MNTB; "EI" input).

Although the loss of temporal coding with increasing sound frequency usually is considered a consequence of the degradation of phase-locking, the notion that reduced temporal performance at higher frequencies represents an intrinsic limitation in neural sensitivity to high stimulation rates reckons without the concept of efficiency. Efficiency represents a fundamental principle of sensory coding whereby neural filters are matched to the statistics of ecologically relevant stimuli. In accordance with this principle, it has been shown in the early auditory system that cochlear and auditory nerve filter characteristics are well-suited to extract the spectrotemporal features present in natural sounds (9, 10). Furthermore, behaviorally relevant stimuli combined with background noise typically display a decreasing signal-to-noise ratio (SNR) with increasing frequency (11). Because the auditory pathways are organized according to sound frequency (tonotopy), this decrease in SNR might be expected to affect the
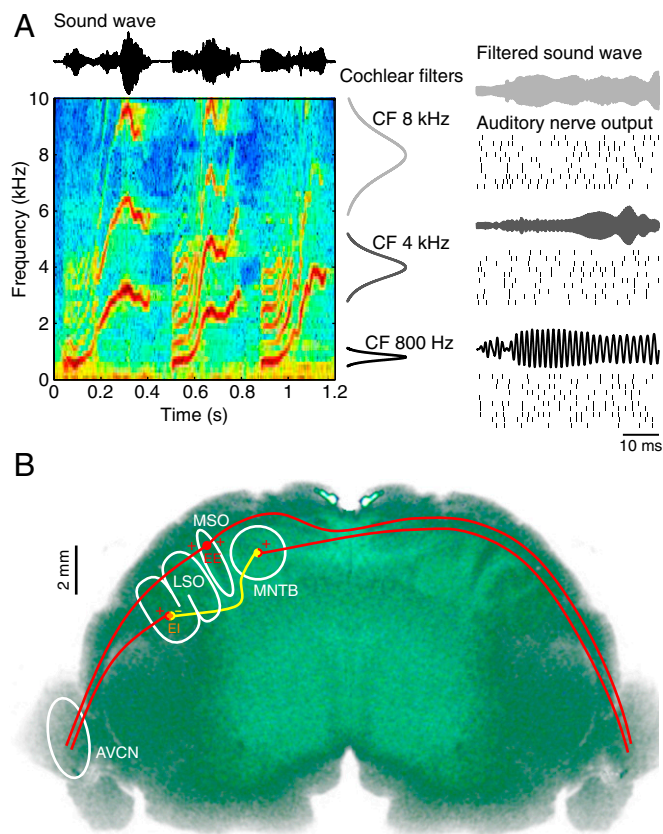
Fig. 1. Peripheral processing of auditory stimuli. (*A*) Guinea pig vocalization sound wave and its spectrogram (*Left*) and the frequency ranges of the spectrogram that are passed by cochlear filters with center frequencies (CFs) of 800 Hz (*Bottom*), 4 kHz (*Middle*), and 8 kHz (*Top*). (*Right*) Examples of auditory nerve responses to 50-ms fragments of the sound wave; 10 realizations of the spike output were produced by using the model from Zilany et al. (66) for auditory nerves with CFs of 800 Hz (*Bottom*), 4 kHz (*Middle*), and 8 kHz (*Top*). (*B*) Horizontal section of the guinea pig brainstem with a schematic of the projections to the MSO and LSO (shown for one side of the brainstem). The MSO receives bilateral excitatory input (i.e., EE input) from the anterior ventral cochlear nuclei (AVCN). The LSO nucleus receives ipsilateral excitatory input from the AVCN and contralateral inhibitory input from the MNTB, which receives excitatory input from the contralateral AVCN (hence, LSO cells receive EI input). Note that the right-hand side of the slice is a reflected copy of the left-hand, recorded, side.

form of the neural code along the frequency axis. To this end, constraints of efficiency are likely to affect the neural representation of spatial cues by MSO and LSO neurons.

Specifically, under the efficiency paradigm, it might be expected that the coding strategies of MSO and LSO neurons are specialized to extract information conveyed by low- and high-frequency components of natural sound. To test this hypothesis, we used in vitro electrophysiological recordings (in guinea pig and rat) to characterize the intrinsic filtering properties of MSO and LSO neurons. We first determined their subthreshold membrane impedance profiles (12, 13) and found strong subthreshold resonance in MSO neurons as well as some neurons in the lateral limb of the LSO (where neurons sensitive to low-frequency sounds are situated) but largely low-pass impedance profiles in the medial limb of the LSO (the location of neurons sensitive to high-frequency sounds). Based on these observed filter properties, we developed a biophysically inspired binaural model and examined its ability to extract spatial information from natural sounds (conspecific vocalizations). We demonstrated that high-frequency resonances contribute to the efficient extraction of ITD cues from

the TFS of low-frequency sounds, whereas neurons with low-pass impedance characteristics coded ILD cues from high-frequency sounds more efficiently. Furthermore, we showed that the change in coding strategy enhances the extraction of spatial information in background noise as the SNR decreases with increasing sound frequency.

Here, we demonstrate a transformation in intrinsic electrical properties of neurons along the main tonotopic axis of the binaural brainstem nuclei that is tuned to exploit the transition in coding information from one emphasizing the TFS of sounds to one emphasizing the temporal envelope.

Results

In Vitro Whole-Cell Recordings from Principal Neurons of MSO and LSO. To determine whether the intrinsic properties of brainstem auditory neurons accord with the efficiency hypothesis, we first characterized the subthreshold input filtering properties of MSO and LSO neurons by performing in vitro whole-cell patch-clamp recordings from these cells in guinea pig brainstem slices at near-physiological temperatures (*Materials and Methods*). The guinea pig was selected as an animal model because, unlike most rodents, its hearing range (14) spans the range of frequencies over which processing shifts from one associated with the TFS (5, 15) to one associated with the temporal envelope (8).

To characterize the neural filters, we determined the subthreshold membrane impedance profile (i.e., the frequency-dependent voltage response) by recording the voltage response to a ZAP current (12, 13), i.e., a sinusoidal current with constant amplitude and linearly increasing frequency (1–1,000 Hz for 0.96 s). When necessary, current was injected to maintain the baseline membrane voltage close to −55 mV (−53 ± 5 mV, $n =$ 17). The amplitude of the ZAP current was adjusted to keep perturbations of the membrane potential close to 5 mV peak to peak, thus avoiding the triggering of action potentials. Fig. 2*Aa* shows the input current (*Upper*) and voltage output (*Lower*) recorded from a guinea pig MSO neuron. The impedance profile (Fig. 2*Ac*) was obtained by dividing the Fourier transform of the voltage response by that of the input current (Fig. 2*Ab*; panels show power spectra). According to their impedance profiles, neurons were classified as "resonant" if they showed a peak in their impedance that was higher than their input resistance (i.e., the impedance to a dc input). Neurons were classified as "low-pass" if such a peak was absent. Resonance peaks were characterized by both the frequency at which they occurred and the quality or "Q factor" (maximum impedance divided by the input resistance; *Materials and Methods*). The presence of a resonance peak implies that a neuron responds preferentially (i.e., the subthreshold voltage response is largest) to inputs whose frequency content matches that of the resonant peak, whereas a low-pass neuron responds better to slowly varying input signals allowing integration of inputs in time (13).

MSO neurons had significantly lower input resistance than LSO neurons (19 ± 3 MΩ with $n = 10$ vs. 73 ± 17 MΩ with $n = 7$; unpaired t test; $P < 0.05$). This difference is the result, at least in part, of the greater activation in MSO neurons of voltage-dependent, low-threshold conductances around the resting membrane potential (16). Most importantly, principal neurons displayed a gradient in their resonant properties along the tonotopic dimension of the MSO and LSO (i.e., MSO to lateral LSO to medial LSO; Fig. 2*B*). All MSO neurons recorded showed a resonance with peak frequencies ranging from 80 to 400 Hz (Fig. 2*C*). Two of three recorded neurons in the LSO's lateral (low-frequency) limb were resonant (Fig. 2*B*, *Center*, triangles in white region of LSO), whereas the four recorded neurons in the medial LSO had low-pass impedance profiles (Fig. 2*B*, triangles in gray region). To demonstrate the generality of this phenomenon further, we evaluated the filtering properties of LSO neurons in the rat, a species with less-well developed low-frequency
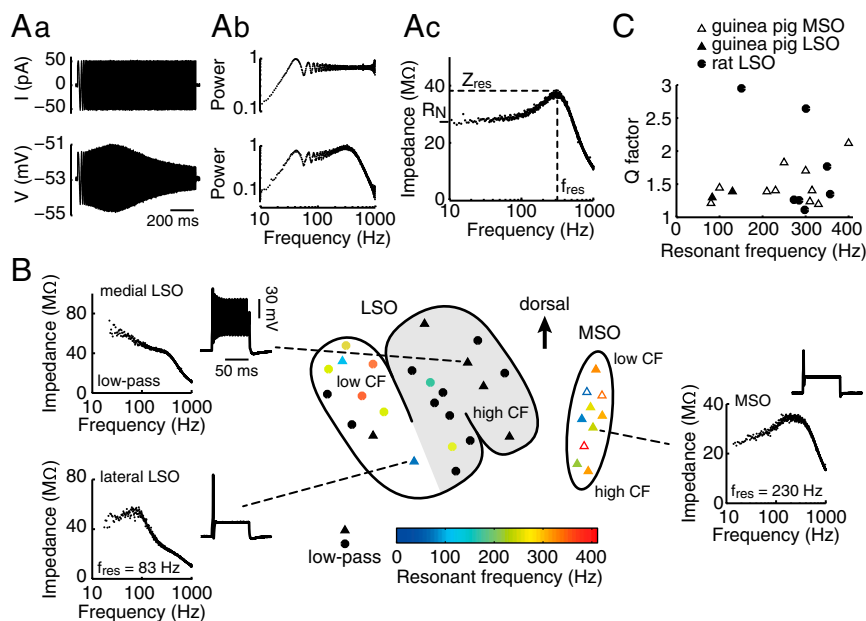
Fig. 2. Assessing intrinsic electrical properties of MSO/LSO neurons. (*Aa*–*Ac*) Illustration of the ZAP protocol applied to a guinea pig MSO cell: (*Aa*) input current and voltage response, (*Ab*) their respective power spectra, and (*Ac*) the impedance profile. Dashed lines in *Ac* indicate the peak resonant frequency (f_{res}) at which impedance is maximal (Z_{res}). The input resistance (R_N) of this cell is indicated on the vertical axis. (*B*) Schematic of LSO and MSO nuclei with the approximate locations of all the recorded cells in the guinea pig MSO and LSO nuclei (▲, △) and rat LSO nucleus (●), color-coded for peak resonant frequency. Black symbols denote nonresonant cells. The △s in the MSO nucleus denote cells for which the precise location within the MSO could not be established. The gray area in the LSO schematic distinguishes the medial and mediolateral limbs from the lateral limb. Shown are three examples of impedance profiles and related spike responses. (*C*) Q factor vs. peak resonant frequency of all resonant MSO and LSO cells. The Q factor is defined as the peak impedance (Z_{res}) divided by the input resistance (R_N; see *A*).

hearing and a less well-defined MSO (17). Input resistances of neurons in the lateral and medial/mediolateral limbs of the rat LSO were not significantly different (112 ± 17 MΩ with $n = 7$ vs. 99 ± 15 MΩ with $n = 10$, respectively). Nevertheless, similar to the guinea pig, most of the neurons (5 of 7) in the lateral LSO limb were resonant, with peak frequencies ranging from 150 to 360 Hz, whereas most of the neurons (8 of 10) in the medial and mediolateral limbs of the rat LSO were low pass. The close correspondence between the impedance profiles of MSO and LSO principal neurons and their presumed sound-frequency tuning suggests that these filtering properties might play an important role in the efficient coding of sound signals across the tonotopic axis.

We also characterized MSO and LSO principal neurons according to their firing properties by injecting suprathreshold current steps through the recording electrode. Consistent with previous reports (18, 19), MSO neurons responded with a single action potential at stimulus onset, i.e., a phasic firing pattern (Fig. 2*B*, *Right*), whereas the responses of LSO neurons were more varied: in the lateral LSO limb, action potentials generally were confined to stimulus onset (Fig. 2*B*, *Lower Left*), whereas those in the medial LSO limb were characterized by a tonic firing pattern (Fig. 2*B*, *Upper Left*).

Modeling Binaural Neurons. We used the filter properties recorded experimentally to develop functional models of binaural neurons to assess their ITD and ILD sensitivity to real-world acoustic inputs. ZAP current responses of the 10 MSO cells and 7 LSO cells from the guinea pig were fitted with linear models describing the subthreshold voltage dynamics. The three examples in Fig. 3*A* illustrate the range of impedance profiles of models fit to data: a low-pass model from the medial LSO, a model with low resonant frequency from the lateral LSO, and a model with a high resonant frequency from the MSO. None of the 17 cells could be fit properly by a simple RC circuit (i.e., a resistance and a capacitance in parallel); the model fits required one or two linearly

voltage-dependent ion currents: a resonant current and/or an amplifying current (*Materials and Methods*; ref. 13). The model fits of the resonant neurons and of one low-pass neuron included a resonant current (g_w; Fig. 3*B*). The parameters of the fitted models suggest that with increasing resonance frequency, a resonant current increases in amplitude, whereas its activation time constant decreases down to ∼0.3 ms (τ_w; Fig. 3*B*). This restorative current contributes strongly to the subthreshold membrane dynamics and has a fast activation time constant, features shared by the low-threshold potassium current (carried by Kv1.1 channels) that is prominent in principal MSO neurons (16, 18) and in a subpopulation of principal LSO neurons (19). The model fits of all low-pass neurons and two of the resonant neurons included an amplifying current (g_n; Fig. 3*C*) with an activation time constant between 0.6 and 1.8 ms (τ_n; Fig. 3*C*). Such a subthreshold amplifying current might reflect a (persistent) sodium current, a low-threshold calcium current, or an inward-rectifying potassium current (see refs. 20, 21).

Modeling ITD and ILD Sensitivity for Resonant and Nonresonant Binaural Neurons. We characterized the influence of model neurons' filtering properties on the sensitivity to ITD and ILD cues conveyed in guinea pig vocalizations. By using a 5-s exemplar of a guinea pig vocalization (Fig. 4*A*), auditory nerve model firing patterns were generated for different frequency components for ipsilateral and contralateral signals to produce synaptic inputs that were then applied to modeled binaural neurons.

We first assessed the responses of model neurons when only the ITD cues were presented. Fig. 4*B* illustrates the activity of auditory nerves, which provide the binaural excitatory (EE) synaptic input to the model neurons. Shown are responses of auditory nerves with center frequencies (CFs; sound frequency for which a neuron has the lowest threshold for evoking action potentials) of 800 Hz (*Left*) when there is phase-locking to the TFS, and with CFs of 8 kHz (*Right*) when auditory nerve activity is not synchronized
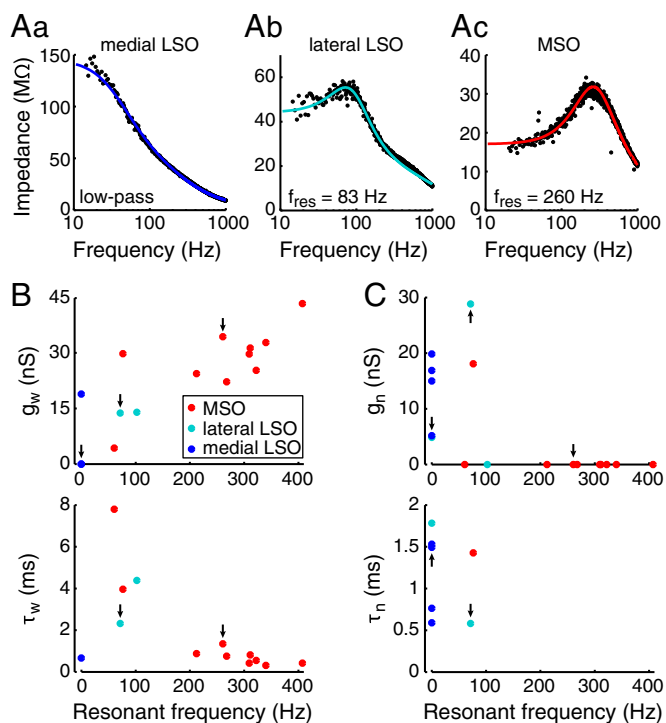
Fig. 3. Linear models predict membrane properties that underlie sub-threshold response of MSO and LSO cells. (*Aa–Ac*) Examples of model fits to principal cells from the guinea pig MSO and LSO: (*Aa*) a low-pass filter from the medial LSO, (*Ab*) a model with low resonant frequency from the lateral LSO, and (*Ac*) a model with high resonant frequency from the MSO. The ●s give the experimentally determined impedance profiles, and solid curves give the model fits. (*B*) Magnitude (g_w in nanosiemens; *Upper*) and activation time constant (τ_w in milliseconds; *Lower*) of the resonant current (*Materials and Methods*) of the cell models, plotted as a function of resonant frequency (low-pass models are plotted at $f_{res} = 0$ Hz). All 12 resonant models and one of the five low-pass models included a resonant current. Arrows indicate models from *A*. (*C*) Magnitude (g_n; *Upper*) and activation time constant (τ_n; *Lower*) of the amplifying current plotted as a function of resonant frequency. All five low-pass models and two of the 12 resonant models contained an amplifying current. Arrows indicate models from *A*.

to the TFS. To model neuronal firing, two mechanisms for generating action potentials ("spikes") were assessed. Spikes were evoked either by crossings of a voltage threshold (v) or by a sufficiently fast rise in the membrane voltage over time (a slope threshold, dv/dt). Note that this slope threshold was an idealization of a mechanism underlying the phasic firing we observed in MSO neurons (and some of the LSO neurons) and also has been reported in other neurons of the auditory brainstem (22, 23). The voltage (or slope) threshold for spike generation was set such that the variation of the output rate of the model neuron was maximized (Fig. 4*C*). Model neurons were assumed to be maximally responsive when the ITD was equivalent to the maximum ITD reported for the guinea pig, i.e., leading by 330 μs relative to the opposite ear (24). The ITD-dependent firing rate was assessed over a 1-ms range, encompassing the maximum range of ITDs over which a neuron's response might vary (i.e., from 330 μs leading at the ipsilateral ear to 330 μs leading at the contralateral ear). Fig. 4*D* compares response variations produced by either slope or voltage threshold. Consistent with previous reports (25), spike generation initiated by a fast rise in voltage elicits greater variations in the response to ITD than does the magnitude of the voltage per se.

ITD sensitivity was assessed for three models (Fig. 3*A*)—"fast" resonant (MSO), "slow" resonant (lateral LSO), and "low-pass"

(medial LSO)—across the frequency range encompassed by the exemplar vocalization (Fig. 4*A*). The fast resonant model always performs better than the slow resonant or low-pass model with respect to variation of the spike rate with ITD (Fig. 4 *E* and *F*). Note that the variation of these sensitivities with CF reflects the wavelength of sound components passing through the filter band, as well as head size (obviously, where signal energy is low or absent there also is little variation in the response). ITD sensitivity shows two clear maxima over different frequency ranges (Fig. 4*E*). The first maximum is explained by considering that ITD sensitivity is cyclic on the period of a pure tone stimulus (or quasiperiodic for broadband sounds; Fig. 4*D*). Therefore, variation of spike rates over a fixed range of ITDs (here, 0 vs. 660 μs) is necessarily frequency dependent and thus is lower for lower sound frequencies (here, <300 Hz). In fact, signal power at 100 Hz and 500 Hz is roughly equal in the exemplar stimulus (Fig. 4*A*, *Lower*), but ITD sensitivity is much greater at the higher frequency. With increasing CF of the auditory nerves, and particularly where phase-locking of monaural inputs to the TFS remains high (500–1,000 Hz), ITD sensitivity is high. At still-higher sound frequencies, however, at which phase-locking to the TFS begins to decline, ITD sensitivity also declines whereupon, above ~2 kHz, it again starts increasing (particularly over the frequency range 5–8 kHz), but this time associated with ITDs conveyed in the sound envelope. Because the cochlear filters broaden with increasing CF (Fig. 1*A*), the range of possible amplitude modulation frequencies also increases with CF, allowing for increased (envelope) ITD sensitivity. This is analogous to the increase in ITD sensitivity to the TFS in the CF range up to 800 Hz. Note, however, because of the low-pass characteristics of the envelope spectrum within high-frequency auditory channels (a product of the filter bandwidths and 1/f characteristics of the envelope power spectrum; Fig. 5 *B* and *C*), envelope ITD sensitivity never approaches that observed for the TFS, even for the fastest resonance model, and declines steadily above 8 kHz.

Model responses also were assessed for the ILD cue alone (Fig. 4 *G–I*). In this case, synaptic stimuli were applied to the neural models by means of ipsilateral excitatory input and contralateral inhibitory input (EI) that mimics LSO connectivity (Fig. 1*B*), yielding model output that is maximal for stimuli from the ipsilateral side (negative ILD, Fig. 4*G*). Fig. 4*H* illustrates that there is little ILD-dependent change in spike rate at low CF; there is little head shadow generated at these frequencies in the guinea pig and, therefore, little ILD (see the idealized relationship between ILD and sound frequency in Fig. 4*G*, *Inset*). With increasing CF, however, the magnitude of the ILD increases as does, concomitantly, the ILD-dependent variation in spike rate. Note, however, that in contrast to ITD, ILD sensitivity is greatest for model neurons incorporating low-pass electrical characteristics (medial LSO model, Fig. 4 *H* and *I*) combined with a spiking mechanism using a voltage threshold. Note, too, that the frequency range over which the maximum ILD-dependent variation in spike rate occurs does not correspond to any particular peak in the vocalization spectrum (compare Fig. 4*H* with Fig. 4*A*).

Contribution of Resonance Properties to Listening in Noise. A critical feature of spatial listening is the ability to hear out sounds against background noise (e.g., competing sources, environmental sounds, or reflections from hard surfaces). Typically, the power of behaviorally relevant signals decreases with increasing frequency (*Insets* in Fig. 5 *E* and *H*), whereas interfering noise often shows a broader power spectrum (11), resulting in unfavorable SNRs with increasing frequency. To this end, we assessed the ability of model neurons to extract spatial cues at different SNRs when both ITD and ILD cues potentially are available (Fig. 5 *A*, *D*, and *G*), considering the 800-Hz and 8-kHz centered energy band as above, as well as an additional, intermediate band centered on 4 kHz. This intermediate band is of special interest because neurons in the LSO encode ITDs both in the TFS and in the envelope by
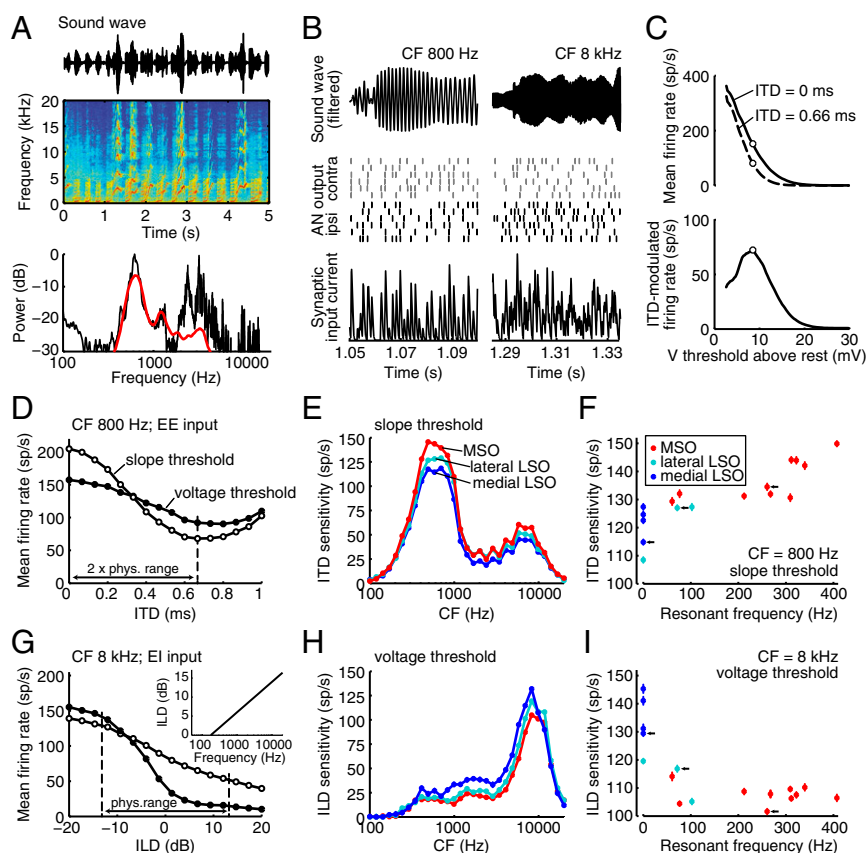
Fig. 4. Sensitivity of model neurons to binaural spatial cues. (*A*) Five-second exemplar of guinea pig vocalization—sound wave (*Top*), spectrogram (*Middle*), and power spectra (*Bottom*) of the exemplar (black) and average of 1,000 conspecific vocalizations (red). (*B*) Synaptic inputs to model neurons were derived from the exemplar vocalization. (*Top*) Fifty-millisecond sound wave fragments band-pass filtered at 800 Hz and 8 kHz. (*Middle*) Modeled auditory nerve (AN) fiber responses (see ref. 66) activate six ipsi- and six contralateral inputs to MSO/LSO models. (*Bottom*) Summed synaptic currents when all 12 inputs are excitatory (EE input). (*C*) Spike output of model cells results from voltage (or voltage slope) threshold crossings. Threshold was chosen such that the output rate modulation was maximized (*Materials and Methods*). (*Upper*) Output rate of the MSO model from Fig. 3*A* as a function of voltage threshold for ITD = 0 or 0.66 ms (i.e., ± physiological range of 0.33 ms). (*Lower*) Difference between the ITD curves shows voltage threshold (○) generating maximum ITD-modulated firing rate. (*D*) Modulation of firing rate with ITD over the range 0–1 ms for a fast resonant model (MSO model in Fig. 3*A*) using a slope threshold (○) or voltage threshold (●). AN input as in C. (*E*) Modulation of firing rate (ITD sensitivity) over ± physiological range (see *D*) as a function of CF of AN fibers using the 5-s exemplar vocalization from *A*. The fast resonant MSO model (red), slow resonant lateral LSO model (cyan), and low-pass medial LSO model (dark blue) are as in Fig. 3*A*. AN fibers provide EE input, and cell models use a slope threshold. Data points plot an average of 60 trials, with error bars indicating SE (largely hidden by symbols). (*F*) ITD sensitivity as a function of peak resonant frequency of all 17 cell models. AN fibers have CF = 800 Hz and provide EE input. Models use a slope threshold. Arrows indicate the three models used in *E*. Error bars show SE for the 60 trials. (*G*) Modulation of firing rate with ILD (without ITD cues) for a low-pass model (medial LSO model from Fig. 3*A*) for slope threshold (○) or voltage threshold (●) spike mechanisms. AN fibers have a CF of 8 kHz and provide excitatory ipsilateral input and inhibitory contralateral (EI) input. (*Inset*) Maximum ILD as a function of sound frequency for the guinea pig (idealization of data in ref. 24). (*H*) Modulation of firing rate (ILD sensitivity) as a function of the CF of the AN fibers using the 5-s exemplar vocalization from *A* for the same three models as in *E*. AN fibers provide EI input, and cell models use a voltage threshold. Data points show the average of 60 trials, with error bars indicating SE (largely hidden by symbols). (*I*) ILD sensitivity as a function of peak resonant frequency of all 17 cell models. AN fibers have CF = 8 kHz and provide EI input. Models use a voltage threshold. Arrows indicate the three models used in *H*. Error bars show SE for the 60 trials.

virtue of their EI inputs (26, 27), suggesting the capacity of these neurons to compute ILD or ITD (or both) for frequencies above a few kilohertz, at which both binaural cues potentially are available. Once more, we assessed the extent to which the two main categories of binaural integration (EE and EI) and spike generation mechanisms (slope and voltage threshold) operate with respect to the three models: fast resonance, slow resonance, and low-pass. Note that we did not include in our model the additional, fast-acting glycinergic inhibitory input posited as contributing to the ITD sensitivity of low-frequency neurons classed as EE in their response type (28, 29), as its biophysical properties remain to be determined.

In general, model neurons with exclusively EE inputs (Fig. 5 *B*, *E*, and *H*) perform best (i.e., the variation in response rate is highest) when they incorporate fast resonance (red curves) and when spike generation is initiated by a slope threshold (triangles

indicate performance with the voltage threshold at +30 dB SNR). Note that the form of the spike generator clearly contributes to the modulation of the neural response. Overall, its contribution (Fig. 5 *B*, *E*, and *H*; differences between triangles and corresponding circles at +30 dB SNR) is of a magnitude similar to the contribution of the subthreshold membrane properties (the difference between triangles or between circles at +30 dB SNR). The extent to which models with fast resonances outperform the other models—evident at high SNRs—is frequency dependent, being most obvious at 800 Hz (Fig. 5*B*), less so at 4 kHz (Fig. 5*E*), and largely absent at 8 kHz (Fig. 5*H*). Note that at 800 Hz, performance is dominated by sensitivity to ITDs conveyed in the TFS and that ITD sensitivity extends down to negative SNRs for all models. This result is consistent with previous studies showing that low-frequency neurons in the guinea pig midbrain encode ITD information at negative SNRs (30). At 4 kHz, model
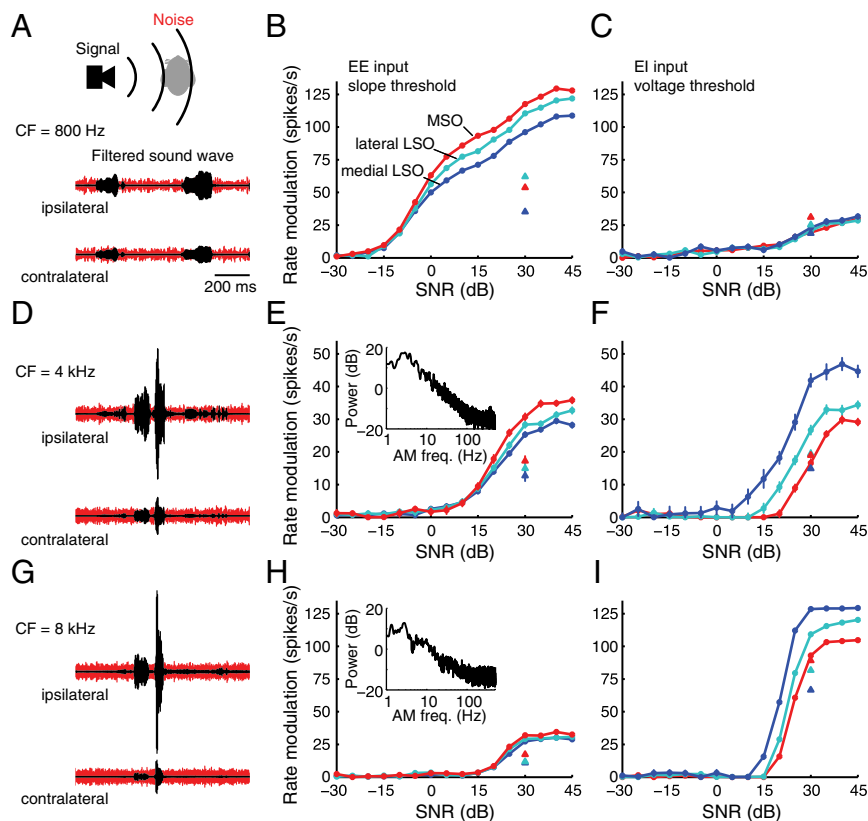
Fig. 5. Sensitivity to combined ITD and ILD cues at low, middle, and high frequencies in a noisy environment. (*A–I*) Gaussian white noise is added to the 5-s exemplar guinea pig vocalization (see Fig. 4*A*) such that the SNR varies from −30 to 45 dB within the frequency bands around 800 Hz (*A–C*; 700–900 Hz), 4 kHz (*D–F*; 3.5–4.5 kHz), and 8 kHz (*G–I*; 7–9 kHz). Firing rate modulation of a fast resonant (MSO, red), a slow resonant (lateral LSO, cyan), and a low-pass model (medial LSO, dark blue) was determined for the vocalization stimulus coming from the ipsilateral side and compared with that coming from the contralateral side. ITD differs by twice the physiological range (±0.33 ms) with the peak of the ITD response function at the ipsilateral side. ILD varies with frequency according to Fig. 4*G*, *Inset*. The noise is uncorrelated for the two ears and does not provide ILD (or ITD) cues. (*A*, *D*, and *G*) For all three frequencies, the ipsilateral and contralateral cochlear filter output is shown for a 500-ms fragment of the vocalization signal (black) and the noise (red) for SNR = 0 dB, where the vocalization signal is presented at the ipsilateral side. (*B*, *C*, *E*, *F*, *H*, and *I*) Firing rate modulation is plotted as a function of the SNR when the three models receive EE input (*B*, *E*, and *H*) or EI input (*C*, *F*, and *I*). Firing rate output is determined by a slope threshold (*B*, *E*, and *H*) or by a voltage threshold (*C*, *F*, and *I*). For comparison, the modulation of the firing rate with the alternate threshold mechanism is indicated at +30 dB SNR by ▲s. (*E* and *H*, *Insets*) Amplitude modulation spectrum of the vocalization in the 4-kHz band (*E*) and 8-kHz band (*H*). Error bars denote SE for 60 trials.

performance is dominated by the (envelope) ITD cue, and although the fast resonance model once again performs best, no model demonstrates variation of the response rate at negative SNRs. At 8 kHz, response rate variation is virtually indistinguishable among the three models for exclusively excitatory inputs and is evident only at relatively high, positive SNRs.

Conversely, model neurons with EI properties (Fig. 5 *C*, *F*, and *I*) perform best when comprising low-pass electrical properties (dark blue curves) and spikes are initiated by crossing a voltage threshold (triangles indicate performance with the slope threshold at +30 dB SNR). The relatively poor sensitivity at 800 Hz (Fig. 5*C*) reflects the lack of ILD cues at this frequency (at least for far-field sources; *Discussion*), but EI models at both 4 kHz (Fig. 5*F*) and 8 kHz (Fig. 5*I*) demonstrate a preference for low-pass electrical characteristics; response rate variation always is greatest for the low-pass model. Nevertheless, performance never achieves that observed at 800 Hz for the EE model at any frequency in that response variation is restricted to positive SNRs. This lack of performance at negative SNRs is consistent with behavioral observations of the relatively limited access to temporal information conveyed in the envelopes of high-frequency sounds and the difficulties associated with listening in noisy or reverberant environments when access to low-frequency TFS is limited (31). Importantly, for the 4-kHz band, there appears to be some benefit from implementing both forms

of model neuron—EE with fast resonance and EI with low-pass electrical characteristics—with regard to rate modulation.

Discussion

We have demonstrated a postsynaptic specialization in electrical resonant properties of auditory brainstem neurons that varies across the tonotopic axis (Fig. 2). Using biophysically inspired binaural neuron models (Fig. 3), we show that these electrical properties contribute to a transition in the coding of temporal information from one emphasizing information conveyed in the fast TFS to one emphasizing information conveyed in the more-slowly changing temporal envelope (Fig. 4). The effect of this change in coding strategy is maintained in the presence of background noise (Fig. 5). Together, the data highlight the efficient coding capacity of brainstem binaural neurons, which appear to be optimized for encoding the statistics of low- and high-frequency components of natural sounds.

Biophysics of Resonance and Effect on Discharge Patterns. Membrane potential resonance has been reported for many neuronal systems (13). In the auditory system, for example, electrical resonance (up to several hundred hertz) underlies hair cell tuning in the turtle cochlea (32). In the mammalian brain, resonances commonly are reported in the range 2–12 Hz and appear to be

related to the generation or maintenance of oscillatory brain waves (e.g., in the hippocampus; ref. 33). Intrinsic low-pass and resonance properties (up to 40 Hz resonances) are evident in the subthreshold responses of vestibular neurons (34), and analogous to our findings, these covary with spiking patterns (phasic or tonic). Therefore, it is unusual, but perhaps not surprising in the context of brain nuclei dedicated to fast, submillisecond temporal coding, to observe resonance frequencies up to several hundred hertz.

Although a range of membrane conductances in principal cells of the MSO and LSO potentially contribute to the appearance of resonances, the most likely contender for the high resonant frequencies reported in the present study is the low-voltage activated potassium channel, particularly Kv1.1. This channel is highly expressed in adult principal cells in the MSO (35, 36), and a tonotopic gradient in the expression of this channel exists across the LSO, decreasing from the lateral to the medial limb (19). The Kv1.1 channel has the characteristics required to produce resonances at high frequencies (>80 Hz) with a large voltage-dependent contribution to the membrane conductance near resting potential and an activation time constant of ~1 ms (35). Note that the hyperpolarization-activated current (I_h), which is responsible for resonances in many neurons in the central nervous system, also is highly expressed in principal MSO and LSO cells (37, 38). However, its slow activation kinetics (~100 ms), which would support resonances only at relatively low frequencies (~10 Hz), means that it cannot account for the high resonant frequencies we report in this study, although I_h may help maintain an operating voltage range so that resonance is preserved (39).

Concomitant with the gradient in Kv1.1 expression reported in LSO in vitro (19), neural firing patterns in the lateral limb tend to respond to injected current steps only at stimulus onset, whereas those in the medial limb respond with a more sustained firing pattern. As onset-firing patterns may be transformed into sustained patterns by blocking the Kv1.1 channel (19), they clearly play an important role in modulating the neural coding strategy in the binaural brainstem nuclei. It is not yet clear, however, exactly how these subthreshold and spiking responses in vitro relate to discharge patterns recorded in vivo. Responses in extracellularly recorded neurons in the LSO typically are characterized as showing a "chopper" response, with regularly spaced peaks of activity following stimulus onset (40, 41). A recent modeling study speculated that Kv1.1 channels might play a role in shaping the dynamics of this chopper activity through its effect on the spike afterhyperpolarization (42). Further modeling work (43) demonstrated that the band-pass filtering by cells with Kv1.1 channels might account for the reduction in firing rate seen in many LSO cell responses to amplitude-modulated tones (presented to the ipsilateral ear) as the modulation rate is increased above a few hundred hertz (44). Note that other factors also might play a role in reducing firing rates (e.g., inhibitory input from MNTB). Most importantly, a recent in vivo study in unanesthetized cats demonstrated that about a third of LSO neurons did not exhibit chopper responses (45) and suggested that these neurons might be located primarily in the lateral LSO—the region where Kv1.1 is expressed most strongly (19). By means of a mathematical model, these authors demonstrated that all types of LSO responses could be reproduced from a modeled chopper cell, depending on the level and latency of ipsilateral inhibition it received. This explanation does not consider, however, whether the different membrane properties of LSO neurons (band-pass vs. low-pass; phasic vs. sustained firing) contribute to the type of discharge pattern observed. Further in vivo experiments might clarify the relationship between Kv1.1 and responses in LSO—for example, through the application of a Kv1.1 blocker such as dendrotoxin.

Resonance and Auditory Spatial Coding. Fast, electrically resonant neurons operating over the low-frequency range would enable the assessment of rapid fluctuations in the TFS at each ear generated by source (or head) movements, as well as changes in the interaural coherence of the sound at each ear resulting from acoustic reflections, reverberation, and the interference patterns generated by multiple, simultaneous sound sources. Sensitivity to all these interaural acoustic features is critical to spatial listening in terms of the identification and localization of sources and in determining features of the source. Conversely, the extent to which ILD cues might be exploited for purposes of sound localization is limited by the size and shape of the head (including the pinnae), at least for sources distant from the listener; ILDs increase as the wavelength of sound decreases (frequency increases) and sufficient head shadow is cast (note, however, that near-field sources also can generate significant ILDs at lower sound frequencies, particularly through interaction with the pinnae, although their role in localization per se remains to be determined; refs. 46–49). Because signal energy falls with increasing sound or modulation frequency (in accordance with the "1/f rule"), sound level and temporal information likely becomes increasingly spurious with increasing sound frequency. Low-pass electrical properties provide for longer temporal integration, improving the accuracy with which level information is assessed. It is worth noting in this regard that thresholds for sound level fall as a function of sound duration and are similar in magnitude to those for ILD. Thus, the predominance of low-pass response characteristics in the high-frequency limb of the LSO favors energy integration over time, presumably to better characterize natural sounds or stimulus features, including at unfavorable SNRs. The data also provide an explanation as to why sensitivity to temporal information in the envelope domain is not robust to interference by background noise (31). The increasingly integrative nature of neurons along the tonotopic axis in response to real-world sounds (here, vocalizations) demonstrates that the concept of efficiency is at play—as the SNR declines with increasing sound frequency, neural performance is enhanced by integrating input over time (neurons showing lower resonance or low-pass electrical behavior) to maximize information. Further, there is some indication that envelope ITDs might be more poorly encoded with increasing CF (ref. 3; although see ref. 50, which calls this into question). Irrespective of the precise limits to performance, however, ITD sensitivity in the high-frequency, envelope domain is relatively restricted compared with that in the low-frequency (<1,500 Hz) domain, and even where it is comparable in conditions of quiet, it is considerably degraded in the presence of interfering signals (51).

It is noteworthy that both resonant and nonresonant neural filters were recorded in the LSO, a structure traditionally considered important for coding ILD and therefore presumably favoring low-pass filtering. Nevertheless, physiological evidence also indicates that LSO neurons encode ITDs in both low- and high-frequency sounds through EI interactions (26, 27, 52), and the two classes of impedance profiles—resonant and nonresonant—might potentially correspond to the neurons encoding ITDs and ILDs, respectively. Regardless of their correspondence, however, the existence of two forms of binaural integration, potentially over the same sound-frequency range, makes sense from a coding perspective. ILDs increase with increasing sound frequency and therefore likely represent the more salient spatial cue at increasingly higher frequencies. However, for many small mammals, the ability to exploit ILDs will be severely limited by the size of their head. Even for species such as the guinea pig, with good low-frequency hearing (14) and the ability to encode fine-structure ITDs (15), peripheral sensitivity to the TFS will have declined (with increasing sound frequency; ref. 5) well before any appreciable ILD cue is present, at least for far-field sources. For the rat, with relatively poor low-frequency hearing (53) compared with the guinea pig, appreciable ILDs may be available only at relatively high frequencies (maximum ILDs are less than 10 dB below 8 kHz; see ref. 49). However, by combining both cues

(envelope ITDs and ILDs) over the same frequency range, it may be possible to overcome the limitations imposed by poor coverage by either cue alone. In this regard, note that neurons in the lateral limb of the LSO of the rat in particular showed high-frequency resonances, consistent with them encoding well temporal information conveyed in the envelopes of (relatively) low-frequency sounds. Finally, note that human listeners show a relative decline in localization performance in the range 3–4 kHz, whereas minimum audible angles increase in midfrequency regions, especially for sources located away from the midline (54, 55). The presence of more complex sounds conveying envelope ITDs may help ameliorate this reduced performance (with pure tones) in at least some real-world listening situations (51, 56).

Evidence of a Tonotopic Gradient in Resonance Properties. Our data suggest a gradient in temporal properties along the tonotopic axis, with highly resonant cells at the tonotopic low-frequency end (MSO and lateral LSO) and low-pass cells at the high-frequency end (medial LSO). Other than the recording position, we have no way to assess in vitro what the sound-frequency tuning of neurons within our slice preparations might be; therefore, we cannot determine whether the transition in resonance frequency, or from resonant to low pass, exists at a more refined level than we report. This is especially so when recordings must be pooled across animals and recording sites fitted to exemplar templates of MSO and LSO structure. Nevertheless, aside from the trend in the data at least being consistent with this notion, other lines of evidence do argue for a more refined gradient in the implementation of resonance properties, chief among this being the reported gradient in the number of cells expressing Kv1.1 across the LSO (19), which would subserve a gradient in the ratio of resonant to low-pass cells across the nucleus. It also should be noted that the MSO likely contains a full representation of the tonotopic gradient (44).

Behaviorally, envelope ITD discrimination performance systematically declines with increasing CF. By 10 kHz, discrimination performance is degraded substantially, or completely absent, at the same modulation frequencies for which performance at 4 kHz is as good as that for low-frequency tones (3). This is mirrored in a decline in the number of brainstem neurons encoding fast temporal modulations with increasing neural CF in the midbrain (8). Because the bandwidth of peripheral cochlear filters increases with the CF, which would favor the opposite outcome, this is consistent with a gradient in temporal processing capacity that runs counter to the tonotopic gradient, the purpose of which may be to best exploit temporal and spatial cues likely to be most informative under natural listening conditions. To this end, the 1/f characteristics of the modulation domain at high frequencies favor low-frequency resonance and low-pass characteristics, at least with respect to maximizing SNR. These seemingly paradoxical, psychoacoustical, and physiological observations, therefore, can be understood in terms of coding efficiency; the systematic reduction in signal energy with increasing frequencies, coupled with the increasing magnitude of ILD cues, favors integrative processes in which temporal precision is sacrificed for improved signal detection through energy integration over time.

Efficient Coding of Auditory Spatial Cues. A critical factor in parsing the contribution of postsynaptic biophysical factors to real-world listening concerns the extent to which neurons' coding capacities are matched to the characteristics of the input stimuli. Given the extremely fast (submillisecond) temporal processing required to follow the TFS of low-frequency sounds in the first place, it is hard to argue that neurons encoding ITD are not efficient. Nevertheless, this is but one feature in the time course of a stimulus that must be encoded, and increasing evidence suggests that auditory neurons extract spectrotemporal cues in an efficient manner (9, 10, 57). In vivo studies indicate that modulation transfer functions of

midbrain neurons become more low pass in the presence of masking noise (58, 59), presumably favoring a range of modulation rates at which the SNR is highest. This suggests that real-time mechanisms contribute to the adaptive capacity of individual auditory neurons to extract relevant signals, and potentially argues in favor of individual neurons exploiting resonant or low-pass properties depending on the listening conditions.

Finally, our data have implications for the restoration of hearing in cochlear implantation, particularly the limitation of negative SNR performance to the TFS domain and the low-pass nature of envelope coding with increasing sound frequency. The ability of human listeners to hear out sounds in background noise is highly dependent on sensitivity to ITDs conveyed in the TFS of low-frequency sounds; in such case, speech recognition thresholds lie in the order of −5 to −10 dB SNR (60). However, most speech processors in cochlear implants remove the TFS from the stimulus, conveying only the more slowly modulated stimulus envelopes to the electrode array, with electrode contacts often confined to more basal, high-frequency aspects of the cochlea. Cochlear implant listeners generally are poor at temporal and spatial hearing tasks (61, 62). Although reasons for such performance deficits likely are multifarious, similar limitations are apparent in acoustic hearing when sounds are filtered to exclude low-frequency pitch and spatial cues; performance for modulation rate and ITD discrimination is relatively labile and largely absent for modulation rates above ~300 Hz (3, 63). Without access to the TFS—specifically through low-frequency channels—the capacity of cochlear implant listeners to extract temporal pitch and spatial cues will remain limited.

Materials and Methods

Slice Preparation. Brain slices were obtained from preweaned rats (P13–P15) or guinea pigs (P1–P14). The experiments were carried out under UK Home Office Project License Number PPL 70/6826, covered by the Animals (Scientific Procedures) Act 1986. After animals were decapitated, the brainstem was dissected out rapidly and attached to agar gel with cyanoacrylate glue (Vetbond; 3M) such that the rostral end was face down. The agar–brainstem combination was mounted on an oscillating tissue slicer (Integraslice 7550 PSDS; Campden Instruments) in oxygenated (95% O_2–5% CO_2) high-sucrose low-sodium artificial cerebrospinal fluid (ACSF; in millimolars: 87 NaCl, 25 NaHCO$_3$, 25 glucose, 2.5 KCl, 1.25 NaH$_2$PO$_4$, 75 sucrose, 0.5 ascorbic acid, 4 MgCl$_2$, 0.5 CaCl$_2$). Horizontal sections 200 μm thick were cut and placed in an incubating bath in oxygenated normal ACSF solution (in millimolars: 125 NaCl, 26 NaHCO$_3$, 25 glucose, 2.4 KCl, 1.1 NaH$_2$PO$_4$, 1 MgCl$_2$, 2 CaCl$_2$) at 35 °C. Slices were cooled to room temperature for at least 1 h.

Electrophysiology. For recording, slices were transferred to a recording chamber mounted in an Olympus BX51W1 upright microscope. The slice was fixed to the bottom of the recording chamber with a nylon grid on a platinum frame. The chamber was perfused constantly with oxygenated normal ACSF solution maintained at 33 ± 2 °C and at a constant rate of 0.29 mL/min by a Gilson Minipuls 3 peristaltic pump. The LSO and MSO were located and centered by using 10× magnification. MSO and LSO principal neurons were identified visually with a 60× objective and during recordings, by their firing properties (46). Neurons were recorded in whole-cell patch-clamp mode with an Axopatch 200B amplifier, low-pass filtered at 10 kHz, digitized at 10–50 kHz with a Digidata 1322A board, and acquired using pClamp 9.2 (Molecular Devices). Glass recording pipettes of 1.5 mm external diameter (World Precision Instruments) were pulled by using a two-stage pipette puller (PC-10 puller; Narishige Group) for resistances of 4–7 MΩ. Micropipettes were filled with a K-gluconate solution containing (in millimolars): 130 Kglu, 5 KCl, 1 EGTA, 2 MgATP, 2 Na$_2$ATP, 0.3 Na$_3$GTP, 10 Hepes, 10 Na$_2$-phosphocreatine. The pipette position was controlled with a Luigs & Neumann SM-5 micromanipulator. After whole-cell configuration was established, resting membrane potential was noted and the firing properties of the neurons were evaluated by applying a series of depolarizing current steps. Cells were accepted for recording only if the resting potential was <−40 mV and action potentials could be elicited upon depolarization. The liquid junction potential was not taken into account. After recording, the position of the recorded cell within the nuclei was assessed by changing the magnification to 10×. In the LSO, the medial and lateral limbs were defined clearly and cells recorded in these areas were classified as medial and lateral, respectively. Cells located between these positions were difficult to classify; therefore, we decided upon a third category (mediolateral) to avoid

introducing extra variability in the other two categories when studying anatomical variations of physiological properties.

ZAP Current Generation and Results Analysis. ZAP current protocols were created with MATLAB. The principal ZAP current protocol used was a sweep from 1 to 1,000 Hz over 0.96 s at a linear rate of increase. Each protocol comprised 10 sweeps at 0.04-s intervals. MATLAB files were exported to pClamp 9 via Excel 2007. ZAP amplitudes were adjusted in pClamp by using the "scale factor" setting to achieve peak membrane potential response amplitudes of ∼5 mV from holding in each cell. The ZAP stimulus and the membrane potential response to the ZAP were subject to a fast Fourier transform (FFT) performed by Clampfit 9 to reveal their respective power spectra with respect to frequency, averaged for the 10 sweeps. Impedance profiles were calculated by dividing the voltage FFT by the current FFT, and the resulting impedance values were plotted as a function of their corresponding frequencies by using GraphPad Prism 5. Q factor was calculated by dividing the value of the impedance at the resonant frequency by the value of a neuron's input resistance (see ref. 64).

Model Fitting and Simulations. Neural models were constructed using the guinea pig experimental data. ZAP current responses of the 10 MSO cells and 7 LSO cells were fitted with a linear membrane-voltage model (see ref. 12). To capture the filtering properties of recorded cells, model fits required not only a capacitive current and a leak current, but also one or two dynamic ion currents: a resonant current and/or an amplifying current (13). Resonant currents function as a negative feedback, counteracting changes in membrane potential, whereas amplifying currents act as a positive feedback, boosting any deviation from the holding potential. The linear model describes the membrane voltage v (in millivolts; note that for convenience, we define the holding potential as 0 mV) and the two types of dynamic membrane currents, and is given by the following system of linear ordinary differential equations:

$$c\frac{dv}{dt} = -g_M\, v - g_w\, w_w + g_n\, w_n + I_{app}(t)$$

$$\tau_w\frac{dw_w}{dt} = v - w_w$$

$$\tau_n\frac{dw_n}{dt} = v - w_n$$

with capacitance c (in picofarads) and total membrane conductance g_M (in nanosiemens). The dynamics of the resonant and amplifying currents with conductance g_w and g_n, respectively (in nanosiemens), are affected by the variables w_w and w_n (in millivolts) with associated time constants τ_w and τ_n, respectively (in milliseconds). The filtering of the applied current I_{app} (in picoamperes) that this system implements can be described by the complex impedance $Z(\omega)$ with radial frequency ω. An expression for $Z(\omega)$ can be obtained from the above system of equations by taking its Fourier transform:

$$\bar{Z}(\omega) = \left(i\omega c + g_M + \frac{g_w}{1 + i\omega\tau_w} - \frac{g_n}{1 + i\omega\tau_n} \right)^{-1},$$

where i is the imaginary unit. Note that input resistance is given by $R_N = Z(\omega = 0) = 1/(g_M + g_w - g_n)$. Parameters of the model were fit to each of the 17 cells by minimizing the summed squared difference of the resistance and reactance (i.e., the real and the imaginary part of the complex impedance, respectively) of the Fourier-transformed experimental data (including input resistance) and of the model (using the functions fmincon and patternsearch from MATLAB). Experimental data were fit using the above model with either a resonant or an amplifying current (total of four parameters). We fit a model with both types of currents (total of six parameters) only

when the fit using one type of current was poor and was greatly improved by including the other current type (the case for one MSO and two LSO cells).

We first used the model fits (from the ZAP data) to predict intrinsic properties of cells, particularly of the voltage-dependent currents shaping subthreshold input filtering. The models subsequently were used to simulate numerically responses to natural sounds and to assess the influence of biophysical properties on coding of interaural cues. A 5-s guinea pig vocalization was used as the exemplar natural stimulus, making sure that its statistics were representative of guinea pig vocalizations (Fig. 4A; recordings provided by M. N. Wallace and J. M. Grimsley, Medical Research Council Institute of Hearing Research, Nottingham, United Kingdom, ref. 65). The peripheral processing of acoustic signals, including the generation of auditory-nerve spike times, was carried out using the model by Zilany et al. (66). This model provides phenomenological descriptions of the major functional components of the auditory periphery, from the middle ear to the auditory nerve. The input of the model is the instantaneous pressure waveform of the stimulus, and the output is the resulting spike times for an auditory nerve fiber with a particular CF. The input first is filtered by the middle ear, then follows three parallel filter paths: two signal paths that describe the basilar membrane filtering and a feed-forward control path that models the effects of outer hair cell function and regulates the gain and bandwidth of the basilar membrane filtering. Both signal filter outputs are passed through inner hair cell transduction functions, the outputs of which are summed and low-pass filtered to produce the inner hair cell receptor potential. This potential drives an inner hair cell–to–auditory nerve synapse model, which subsequently leads to the generation of spikes according to an inhomogeneous Poisson process with refractoriness. MSO and LSO cell models received synaptic input relaying activity from six contralateral and six ipsilateral auditory nerve fibers. By generating the synaptic input directly from the auditory nerve fibers, we are idealizing the cochlear nucleus as a simple relay (see, e.g., ref. 43). Activities of all fibers were independent realizations of the auditory periphery model using identical CF. Ipsilateral input was always excitatory; the shape of the excitatory postsynaptic currents was described by an alpha function with time constant 0.2 ms (67). Contralateral input was either excitatory (leading to EE input) or inhibitory (leading to EI input), with the shape of the inhibitory postsynaptic currents described by the difference of two exponential functions with time constants of 0.2 ms and 2 ms (68). The peak amplitude of an excitatory postsynaptic current was −4.75 times the peak amplitude of an inhibitory postsynaptic current, such that both currents provided an equal amount of charge. Note that the absolute amplitude of the synaptic input was arbitrary because the membrane voltage models are linear. Action potential output of the cell models was computed from voltage traces by setting either a fixed voltage threshold or a slope (dv/dt) threshold and adding a 1-ms refractory period. The slope threshold was an idealization of the mechanism underlying phasic firing (see refs. 22 and 23). The threshold value was set for each model such that modulation of output firing rate was maximal for a particular CF (and dependent on the use of either EE or EI input), ensuring that performance of the models was not limited by an arbitrary choice of a fixed threshold. A minimal voltage or slope threshold was imposed for each model, such that spontaneous activity of the auditory nerve input to the models (i.e., when no acoustic stimulus is presented) produced output firing rates of maximally 10 Hz (this minimal threshold was determined separately for EE and EI input).

1. Rosen S (1992) Temporal information in speech: Acoustic, auditory and linguistic aspects. *Philos Trans R Soc Lond B Biol Sci* 336(1278):367–373.
2. McFadden D, Jeffress LA, Ermey HL (1971) Differences of interaural phase and level in detection and lateralization: 250 Hz. *J Acoust Soc Am* 50(6):1484–1493.
3. Bernstein LR, Trahiotis C (2002) Enhancing sensitivity to interaural delays at high frequencies by using "transposed stimuli." *J Acoust Soc Am* 112(3 Pt 1): 1026–1036.
4. Brughera A, Dunai L, Hartmann WM (2013) Human interaural time difference thresholds for sine tones: The high-frequency limit. *J Acoust Soc Am* 133(5):2839–2855.
5. Palmer AR, Russell IJ (1986) Phase-locking in the cochlear nerve of the guinea-pig and its relation to the receptor potential of inner hair-cells. *Hear Res* 24(1):1–15.
6. Joris PX, Carney LH, Smith PH, Yin TC (1994) Enhancement of neural synchronization in the anteroventral cochlear nucleus. I. Responses to tones at the characteristic frequency. *J Neurophysiol* 71(3):1022–1036.
7. Henning GB (1974) Detectability of interaural delay in high-frequency complex waveforms. *J Acoust Soc Am* 55(1):84–90.
8. Griffin SJ, Bernstein LR, Ingham NJ, McAlpine D (2005) Neural sensitivity to interaural envelope delays in the inferior colliculus of the guinea pig. *J Neurophysiol* 93(6): 3463–3478.
9. Lewicki MS (2002) Efficient coding of natural sounds. *Nat Neurosci* 5(4):356–363.
10. Smith E, Lewicki MS (2005) Efficient coding of time-relative structure using spikes. *Neural Comput* 17(1):19–45.

11. Singh NC, Theunissen FE (2003) Modulation spectra of natural sounds and ethological theories of auditory processing. *J Acoust Soc Am* 114(6 Pt 1):3394–3411.
12. Puil E, Gimbarzevsky B, Miura RM (1986) Quantification of membrane properties of trigeminal root ganglion neurons in guinea pigs. *J Neurophysiol* 55(5):995–1016.
13. Hutcheon B, Yarom Y (2000) Resonance, oscillation and the intrinsic frequency preferences of neurons. *Trends Neurosci* 23(5):216–222.
14. Heffner R, Heffner H, Masterton B (1971) Behavioral measurements of absolute and frequency-difference thresholds in guinea pig. *J Acoust Soc Am* 49(6):1888–1895.
15. McAlpine D, Jiang D, Palmer AR (2001) A neural code for low-frequency sound localization in mammals. *Nat Neurosci* 4(4):396–401.
16. Svirskis G, Dodla R, Rinzel J (2003) Subthreshold outward currents enhance temporal integration in auditory neurons. *Biol Cybern* 89(5):333–340.
17. Smith AJ, Owens S, Forsythe ID (2000) Characterisation of inhibitory and excitatory postsynaptic currents of the rat medial superior olive. *J Physiol* 529(Pt 3):681–698.
18. Svirskis G, Kotak V, Sanes DH, Rinzel J (2002) Enhancement of signal-to-noise ratio and phase locking for small inputs by a low-threshold outward current in auditory neurons. *J Neurosci* 22(24):11019–11025.
19. Barnes-Davies M, Barker MC, Osmani F, Forsythe ID (2004) Kv1 currents mediate a gradient of principal neuron excitability across the tonotopic axis in the rat lateral superior olive. *Eur J Neurosci* 19(2):325–333.
20. Tennigkeit F, Schwarz DW, Puil E (1999) Modulation of frequency selectivity by Na$^+$- and K$^+$-conductances in neurons of auditory thalamus. *Hear Res* 127(1-2):77–85.
21. Leao RM, Li S, Doiron B, Tzounopoulos T (2012) Diverse levels of an inwardly rectifying potassium conductance generate heterogeneous neuronal behavior in a population of dorsal cochlear nucleus pyramidal neurons. *J Neurophysiol* 107(11):3008–3019.
22. McGinley MJ, Oertel D (2006) Rate thresholds determine the precision of temporal integration in principal cells of the ventral cochlear nucleus. *Hear Res* 216-217:52–63.
23. Meng X, Huguet G, Rinzel J (2012) Type III excitability, slope sensitivity and co-incidence detection. *Discrete Contin Dyn Syst Ser A* 32(8):2729–2757.
24. Sterbing SJ, Hartung K, Hoffmann K-P (2003) Spatial tuning to virtual sounds in the inferior colliculus of the guinea pig. *J Neurophysiol* 90(4):2648–2659.
25. Gai Y, Doiron B, Kotak V, Rinzel J (2009) Noise-gated encoding of slow inputs by auditory brain stem neurons with a low-threshold K+ current. *J Neurophysiol* 102(6):3447–3460.
26. Joris PX (1996) Envelope coding in the lateral superior olive. II. Characteristic delays and comparison with responses in the medial superior olive. *J Neurophysiol* 76(4):2137–2156.
27. Tollin DJ, Yin TCT (2005) Interaural phase and level difference sensitivity in low-frequency neurons in the lateral superior olive. *J Neurosci* 25(46):10648–10657.
28. Brand A, Behrend O, Marquardt T, McAlpine D, Grothe B (2002) Precise inhibition is essential for microsecond interaural time difference coding. *Nature* 417(6888):543–547.
29. Pecka M, Brand A, Behrend O, Grothe B (2008) Interaural time difference processing in the mammalian medial superior olive: The role of glycinergic inhibition. *J Neurosci* 28(27):6914–6925.
30. Jiang D, McAlpine D, Palmer AR (1997) Detectability index measures of binaural masking level difference across populations of inferior colliculus neurons. *J Neurosci* 17(23):9331–9339.
31. Rakerd B, Hartmann WM (2010) Localization of sound in rooms. V. Binaural coherence and human sensitivity to interaural time differences in noise. *J Acoust Soc Am* 128(5):3052–3063.
32. Crawford AC, Fettiplace R (1981) An electrical tuning mechanism in turtle cochlear hair cells. *J Physiol* 312:377–412.
33. Buzsáki G (2002) Theta oscillations in the hippocampus. *Neuron* 33(3):325–340.
34. Beraneck M, et al. (2007) Differential intrinsic response dynamics determine synaptic signal processing in frog vestibular neurons. *J Neurosci* 27(16):4283–4296.
35. Scott LL, Mathews PJ, Golding NL (2005) Posthearing developmental refinement of temporal processing in principal neurons of the medial superior olive. *J Neurosci* 25(35):7887–7895.
36. Svirskis G, Kotak V, Sanes DH, Rinzel J (2004) Sodium along with low-threshold potassium currents enhance coincidence detection of subthreshold noisy signals in MSO neurons. *J Neurophysiol* 91(6):2465–2473.
37. Adam TJ, Finlayson PG, Schwarz DW (2001) Membrane properties of principal neurons of the lateral superior olive. *J Neurophysiol* 86(2):922–934.
38. Khurana S, et al. (2012) An essential role for modulation of hyperpolarization-activated current in the development of binaural temporal precision. *J Neurosci* 32(8):2814–2823.
39. Khurana S, Remme MWH, Rinzel J, Golding NL (2011) Dynamic interaction of I_h and $I_{K\text{-}LVA}$ during trains of synaptic potentials in principal neurons of the medial superior olive. *J Neurosci* 31(24):8936–8947.
40. Tsuchitani C (1982) Discharge patterns of cat lateral superior olivary units to ipsilateral tone-burst stimuli. *J Neurophysiol* 47(3):479–500.
41. Tsuchitani C, Johnson DH (1985) The effects of ipsilateral tone burst stimulus level on the discharge patterns of cat lateral superior olivary units. *J Acoust Soc Am* 77(4):1484–1496.
42. Zhou Y, Colburn HS (2010) A modeling study of the effects of membrane after-hyperpolarization on spike interval statistics and on ILD encoding in the lateral superior olive. *J Neurophysiol* 103(5):2355–2371.
43. Wang L, Colburn HS (2012) A modeling study of the responses of the lateral superior olive to ipsilateral sinusoidally amplitude-modulated tones. *J Assoc Res Otolaryngol* 13(2):249–267.
44. Joris PX, Smith PH, Yin TC (1998) Coincidence detection in the auditory system: 50 years after Jeffress. *Neuron* 21(6):1235–1238.
45. Greene NT, Davis KA (2012) Discharge patterns in the lateral superior olive of decerebrate cats. *J Neurophysiol* 108(7):1942–1953.
46. Brungart DS, Rabinowitz WM (1999) Auditory localization of nearby sources. Head-related transfer functions. *J Acoust Soc Am* 106(3 Pt 1):1465–1479.
47. Jones HG, Koka K, Thornton JL, Tollin DJ (2011) Concurrent development of the head and pinnae and the acoustical cues to sound location in a precocious species, the chinchilla (Chinchilla lanigera). *J Assoc Res Otolaryngol* 12(2):127–140.
48. Koka K, Jones HG, Thornton JL, Lupo JE, Tollin DJ (2011) Sound pressure transformations by the head and pinnae of the adult Chinchilla (Chinchilla lanigera). *Hear Res* 272(1-2):135–147.
49. Koka K, Read HL, Tollin DJ (2008) The acoustical cues to sound location in the rat: Measurements of directional transfer functions. *J Acoust Soc Am* 123(6):4297–4309.
50. Majdak P, Laback B (2009) Effects of center frequency and rate on the sensitivity to interaural delay in high-frequency click trains. *J Acoust Soc Am* 125(6):3903–3913.
51. Monaghan JJM, Krumbholz K, Seeber BU (2013) Factors affecting the use of envelope interaural time differences in reverberation. *J Acoust Soc Am* 133(4):2288–2300.
52. Finlayson PG, Caspary DM (1991) Low-frequency neurons in the lateral superior olive exhibit phase-sensitive binaural inhibition. *J Neurophysiol* 65(3):598–605.
53. Heffner HE, Heffner RS, Contos C, Ott T (1994) Audiogram of the hooded Norway rat. *Hear Res* 73(2):244–247.
54. Stevens SS, Newman EB (1936) The localization of actual sources of sound. *Am J Psychol* 48(2):297–306.
55. Mills AW (1958) On the minimum audible angle. *J Acoust Soc Am* 30:237–246.
56. Ruggles D, Bharadwaj H, Shinn-Cunningham BG (2012) Why middle-aged listeners have trouble hearing in everyday settings. *Curr Biol* 22(15):1417–1422.
57. Smith EC, Lewicki MS (2006) Efficient auditory coding. *Nature* 439(7079):978–982.
58. Rees A, Palmer AR (1988) Rate-intensity functions and their modification by broadband noise for neurons in the guinea pig inferior colliculus. *J Acoust Soc Am* 83(4):1488–1498.
59. Lesica NA, Grothe B (2008) Efficient temporal processing of naturalistic sounds. *PLoS One* 3(2):e1655.
60. Plomp R, Mimpen AM (1979) Improving the reliability of testing the speech reception threshold for sentences. *Audiology* 18(1):43–52.
61. Zeng FG (2002) Temporal pitch in electric hearing. *Hear Res* 174(1-2):101–106.
62. Seeber BU, Fastl H (2008) Localization cues with bilateral cochlear implants. *J Acoust Soc Am* 123(2):1030–1042.
63. Akeroyd MA, Patterson RD (1997) A comparison of detection and discrimination of temporal asymmetry in amplitude modulation. *J Acoust Soc Am* 101(1):430–439.
64. Hutcheon B, Miura RM, Puil E (1996) Subthreshold membrane resonance in neocortical neurons. *J Neurophysiol* 76(2):683–697.
65. Grimsley JMS, Palmer AR, Wallace MN (2011) Age differences in the purr call distinguished by units in the adult guinea pig primary auditory cortex. *Hear Res* 277(1-2):134–142.
66. Zilany MSA, Bruce IC, Nelson PC, Carney LH (2009) A phenomenological model of the synapse between the inner hair cell and auditory nerve: Long-term adaptation with power-law dynamics. *J Acoust Soc Am* 126(5):2390–2412.
67. Couchman K, Grothe B, Felmy F (2010) Medial superior olivary neurons receive surprisingly few excitatory and inhibitory inputs with balanced strength and short-term dynamics. *J Neurosci* 30(50):17111–17121.
68. Magnusson AK, Kapfer C, Grothe B, Koch U (2005) Maturation of glycinergic inhibition in the gerbil medial superior olive after hearing onset. *J Physiol* 568(Pt 2):497–512.